

## Special Topic

# Review of recent experimental and modeling advances in the understanding of lower hybrid current drive in ITER-relevant regimes

B.J. Ding<sup>1</sup>, P.T. Bonoli<sup>2</sup>, A. Tuccillo<sup>3</sup>, M. Goniche<sup>4</sup>, K. Kirov<sup>5</sup>, M. Li<sup>1</sup> , Y. Li<sup>1</sup>, R. Cesario<sup>3</sup>, Y. Peysson<sup>4</sup>, A. Ekedahl<sup>4</sup>, L. Amicucci<sup>3</sup>, S. Baek<sup>2</sup>, I. Faust<sup>2</sup>, R. Parker<sup>2</sup>, S. Shiraiwa<sup>2</sup>, G.M. Wallace<sup>2</sup>, A. Cardinali<sup>3</sup>, C. Castaldo<sup>3</sup>, S. Ceccuzzi<sup>3</sup>, J. Mailloux<sup>5</sup>, F. Napoli<sup>3</sup>, F. Liu<sup>1</sup>, B. Wan<sup>1</sup> and JET Contributors<sup>6,a</sup>

<sup>1</sup> Institute of Plasma Physics, Chinese Academy of Science, Hefei 230031, China

<sup>2</sup> MIT Plasma Science and Fusion Center, Cambridge, MA 02139, United States of America

<sup>3</sup> ENEA, FSN Department, C. R. Frascati, via E. Fermi 45, 00044 Frascati (Roma), Italy

<sup>4</sup> CEA, IRFM, F-13108, St-Paul-Lez-Durance, France

<sup>5</sup> UKAEA-CCFE, Culham Science Centre, Abingdon, Oxon, OX14 3DB, United Kingdom of Great Britain and Northern Ireland

<sup>6</sup> EUROfusion Consortium, JET, Culham Science Centre, Abingdon, OX14 3DB, United Kingdom of Great Britain and Northern Ireland

E-mail: [bjding@ipp.ac.cn](mailto:bjding@ipp.ac.cn) and [bonoli@psfc.edu.cn](mailto:bonoli@psfc.edu.cn)

Received 12 April 2018, revised 13 June 2018

Accepted for publication 3 July 2018

Published 20 July 2018



## Abstract

Progress in understanding lower hybrid current drive (LHCD) at high density has been made through experiments and modeling, which is encouraging given the need for an efficient off-axis current profile control technique in burning plasma. By reducing the wall recycling of neutrals, the edge temperature is increased and the effect of parametric instability (PI) and collisional absorption (CA) is reduced, which is beneficial for increasing the current drive efficiency. Strong single pass absorption is preferred to prevent CA and high LH operating frequency is essential for wave propagation to the core region at high density, presumably to mitigate the effect of PI. The dimensionless parameter that characterizes LH wave accessibility and wave refraction for the experiments in this joint study is shown to bracket the region in parameter space where ITER LHCD experiments will operate in the steady state scenario phase. Further joint experiments and cross modeling are necessary to understand the LHCD physics in weak damping regimes which would increase confidence in predictions for ITER where the absorption is expected to be strong.

Keywords: lower hybrid current drive, magnetic fusion, ITER

(Some figures may appear in colour only in the online journal)

<sup>a</sup> See the author list of Litaudon *et al* [52].

## 1. Introduction

Lower hybrid current drive (LHCD) has the attractive property of high off-axis ( $r/a \approx 0.7$ ) [1] current drive (CD) efficiency making this a useful technique for broadening the current density profile in order to sustain non-monotonic (shear reversed) profiles of the safety factor— $q(r)$  with  $q_{\min} > 2$  and large shear reversal radius ( $r/a \approx 0.7$ ). Moreover, in H-mode regimes, the onset of instabilities characteristic of the pedestal radial layer (at  $r/a \approx 0.9$ ) would be prevented by the natural current profiles produced by bootstrap effect, which can be efficiently matched by LHCD [2]. This feature would allow exploiting a high fraction of bootstrap current ( $\approx 60\%$ – $70\%$ ), an important condition for viability of an economic fusion reactor [3]. The LHCD tool should be thus considered for the steady state Scenario-4 in the ITER device [4], and for pulsed reactor regimes as well [5, 6]. However, how to improve LHCD capability at high density is an important issue to be solved before this application, which is mainly affected by collisional damping losses when the single pass damping is low, parametric instability (PI), scattering by density fluctuations (SDF), and LH wave accessibility.

In order to investigate physics issues critical for LHCD at reactor relevant densities, a multi-machine assessment, including experiments and modeling in Alcator C-Mod, EAST, FTU, JET, and tore supra (TS) tokamaks, has been continued as a joint activity under the coordination of the integrated operation scenarios (IOS) Topical Group of the ITPA. In these joint experiments the C-Mod and FTU tokamaks are operated at high field magnetic field (5–8 T) and high density ( $5\text{--}20 \times 10^{19} \text{ m}^{-3}$ ), and EAST, JET and TS are operated (for these experiments) at low to medium field (1.8–3.8 T) and lower density ( $2\text{--}4 \times 10^{19} \text{ m}^{-3}$ ). Although these LHCD experiments span more than an order of magnitude in density, about a factor of five in toroidal magnetic field, and correspond to both limited (FTU, TS) and diverted (C-Mod, EAST, JET) discharges, their LHCD parameter regimes can be usefully characterized in terms of electron plasma frequency ( $f_{pe}$ ) to electron gyrofrequency ( $f_{ce}$ ) ratio ( $f_{pe}/f_{ce}$ ) (see figure 1), which is the fundamental dimensionless parameter that determines wave accessibility, wave penetration, and wave refraction. Note that for these experiments ( $f_{pe}/f_{ce}$ ) covers a range from 0.35 to  $\geq 1.0$  which easily brackets the value of 0.5–0.6 expected in the ITER steady state Scenario 4, thus giving some confidence in the extrapolation of results found in these experiments to ITER. In fact, the contour for ( $f_{pe}/f_{ce}$ )  $\approx 0.48$  passes through the operating space of all five devices. In terms of absolute parameters, the C-Mod, EAST, and FTU tokamaks operate with LH source frequencies of 4.6–8.0 GHz, which brackets the source frequency of 5.0 GHz that was planned for ITER. Similarly, both C-Mod and FTU operate at densities of  $0.5\text{--}2.0 \times 10^{20} \text{ m}^{-3}$  and magnetic fields (5–8 T) which bracket the values of  $\sim 0.7 \times 10^{20} \text{ m}^{-3}$  and 5.3 T respectively which are anticipated for the ITER Steady State Scenario 4 [4].

Experiments on FTU identified a new method that enabled LHCD at densities comparable to DEMO [7]. This method was assessed on the basis of previous theoretical predictions

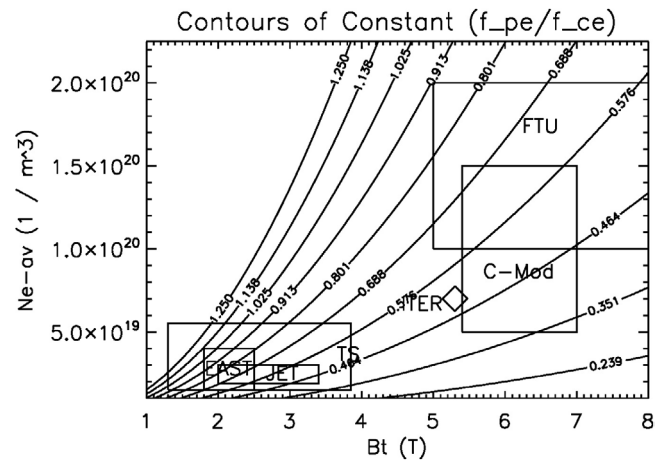


**Figure 1.** Contours of ( $f_{pe}/f_{ce}$ ) for the tokamaks used in the joint study (Alcator C-Mod, EAST, FTU, JET, and TORE SUPRA (TS)).

of diminished parasitic effect of spectral broadening due to PI under higher temperature of plasma edge [8]. In further studies, collisional absorption (CA) [9], and SDF [10, 11], individually or in combination, were also proposed as possible candidates for the CD efficiency decreasing at high density faster than standard theory prediction [12]. Though studies show that SDF and PI can both broaden the initial  $N_{||}$  spectra and affect the CD capability, the mechanisms seem to be essential in terms of achieving agreement between theory and experiment.

The EAST tokamak has both 2.45 GHz and 4.6 GHz LH source power installed which offers the unique capability to study LHCD physics with two different source frequencies applied simultaneously or separately in the same machine. Thus, this manuscript reports also on CD efficiency scaling with source frequency in EAST at fixed density. LHCD experiments performed on the EAST, C-Mod, and FTU devices are typically in the weak damping regime where the injected phase speed is much larger than the phase speed where strong electron Landau damping occurs, i.e.  $v_{||}/v_{te} \gg 2.5$ , where  $v_{te} = (2T_e/m_e)^{0.5}$ . In these experiments, interaction of the LH wave with the cold scrape off layer occurs which can lead to parasitic absorption of the wave power in the edge. The EAST device has the capability to study LHCD physics in this weak damping regime with different edge conditioning techniques such as supersonic molecular beam injection (SMBI), weak lithiation, and strong lithiation, thus testing the effectiveness of these different techniques for mitigating parasitic losses in the SOL.

The Alcator C-Mod tokamak is operated under a wide range of densities and magnetic field which make it possible to study LH CD at the actual absolute values of density and magnetic field anticipated for ITER. Control of the SOL width in C-Mod by increasing the plasma current make it possible to study and mitigate parasitic interactions of the LH wave with the SOL due to PI and CA [13].

Finally the JET tokamak with its significant auxiliary heating power in the form of neutral beam injection (NBI) makes it possible to study far off-axis LHRF power deposition and current generation, which is the ultimate application goal for LHCD in a reactor grade plasma.

As part of these studies computational models for linear and nonlinear wave propagation and absorption are necessary to interpret and analyze experimental results. In order to more accurately capture parasitic interactions of the LH wave with the SOL due to CA we have implemented realistic plasma profiles and SOL geometry in an advanced ray tracing (RT)/Fokker Planck code. In addition the effect of SDF has been included in these models viz. spectral broadening of the power spectrum [14] coupled from the LH waveguide launcher. The importance of edge density profiles in determining the coupled LH launcher spectra [15] has also been investigated and found to be important. Finally an improved parametric dispersion code was used to study nonlinear excitation of the LH wave (sideband) in the parallel coupling limit. In this case the excited sideband LH wave spends longer time at the plasma edge where it is unstable to parametric instabilities.

The manuscript is arranged as follows. In section 2, results from the joint experimental activity are presented, followed by the cross-study and data analysis in section 3. Finally, conclusions and discussion will be given in section 4.

## 2. Results from joint experimental activity

### 2.1. EAST

In this section LHCD experiments on the EAST tokamak are reviewed which emphasize two unique aspects of the facility. First, since the device is superconducting, it is possible to sustain fully noninductive and partially noninductive discharges for long pulse albeit at lower toroidal magnetic field strength of 2–2.8 T, thus allowing access to regimes that test plasma control methods. Second, a 2.45 GHz and 4.6 GHz LHRF system are both installed on EAST, and operate simultaneously or separately, making it possible to unambiguously investigate the physics advantages of higher RF source frequency. EAST experiments aim at fully assessing conditions useful for enabling the LHCD effect into a dense plasma core. As shown in figure 2, first LHCD results [16] with 4.6 GHz show that the lower hybrid wave (LHW) can be coupled to plasma with low reflection coefficient (RC), drive plasma current and plasma rotation, modify the plasma current profile, and heat the plasma efficiently. Meanwhile, good plasma heating is observed with core electron temperature above 4 keV [16].

The effect of lower hybrid (LH) frequency, with  $N_{//}^{\text{peak}} = 2.1$  for 2.45 GHz and  $N_{//}^{\text{peak}} = 2.04$  for 4.6 GHz, on LHCD characteristics at  $n_e = 2.0 \times 10^{19} \text{ m}^{-3}$  with the same coupled power (1.05 MW) in a lower single null (LSN) configuration was investigated in EAST (see figure 3) [17, 18]. Here,  $N_{//}$  is the refractive index parallel to the applied magnetic field and  $N_{//}^{\text{peak}}$  is the peak value. It shows the residual voltages ( $V_{\text{loop}}$ ) are 0.27 V and 0.15 V, respectively, during 2.45 GHz and 4.6 GHz application, possibly implying a higher CD efficiency for the 4.6 GHz LH system. Better plasma heating effect for 4.6 GHz can be seen from the time evolution of plasma stored energy, and central electron temperature ( $T_{e0}$ ) measured with an x-ray crystal spectrometer (XCS) [19]. The internal inductance ( $l_i$ ) is higher with the 4.6 GHz LH wave injection,

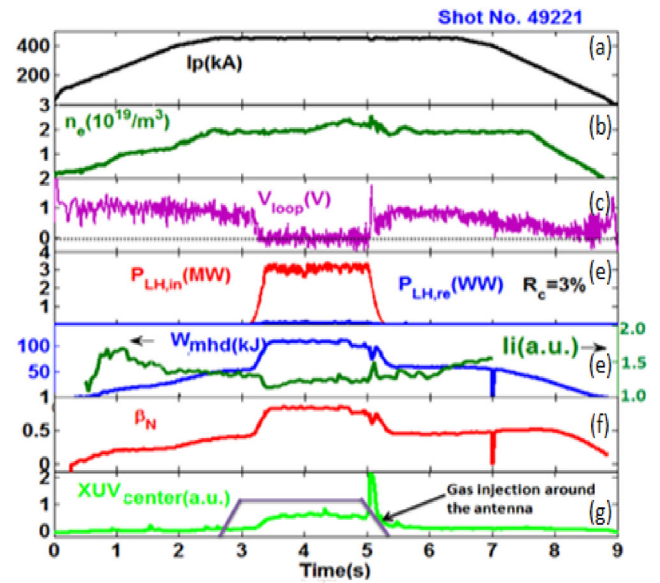


**Figure 2.** Typical waveforms of coupling, CD and plasma heating in EAST for 4.6 GHz LH power injection. (a) Plasma current (kA) versus time (s), (b) line averaged density ( $10^{19} \text{ m}^{-3}$ ) versus time (s), (c) loop voltage (V) versus time (s), (d) injected LH power (MW) in red and reflected LH power (MW) in blue versus time (s), (e) stored energy (kJ) in blue and internal inductance (green) versus time (s), (f)  $\beta_N = \beta_t/[I_p(A)/(a(m))/B(T)]$  versus time (s), (g) XUV (a.u.) at the center (green) and gas injection at the antenna (a.u.) in black versus time (s). Reproduced courtesy of IAEA. Figure from [16]. Copyright 2015 IAEA.

meaning a more peaked current profile. The plasma rotation shows, for similar power input, a larger central rotation change with 4.6 GHz. The increase of heat load on the divertor inferred from the temperature measurement with the infrared camera combined with the increase of the stored energy  $W_{\text{dia}}$  suggests an increase of the LHCD power absorbed by the plasma for the 4.6 GHz antenna.

These experimental results demonstrate that LHWs at 4.6 GHz exhibit stronger CD effect than at 2.45 GHz, which is consistent with less pronounced PI behavior with 4.6 GHz LH wave (see figure 4). However, this difference can also be attributed to a reduction in the power of the main forward lobe at 2.45 GHz relative to 4.6 GHz because of large RCs ( $\approx 10\%$ ) in the 2.45 GHz system (as to be discussed further in section 3.4.2).

By means of simultaneous injection of 4.6 GHz and 2.45 GHz LH power, as shown in figure 5, H-mode is obtained in EAST at relatively high density, even up to  $n_e \sim 4.5 \times 10^{19} \text{ m}^{-3}$ , where a CD effect is still observed, as indicated by the trace for electron cyclotron emission (ECE) located at the major radius of 2.33 m. In this case the higher toroidal magnetic field at the geometric center ( $R = R_0$ ),  $B_0 = 2.8 \text{ T}$ , improves LH wave accessibility for both frequency sources, thus making it possible to penetrate to the higher densities. In particular note from figure 5 the initial loop voltage drop to  $V_{\text{Loop}} \approx 0.35 \text{ V}$  that occurs with application of 2.45 GHz LH power is maintained as the line averaged density continues to ramp up from  $\sim 1.5 \times 10^{19} \text{ m}^{-3}$  to  $4.5 \times 10^{19} \text{ m}^{-3}$  via application of the 4.6 GHz LH power.

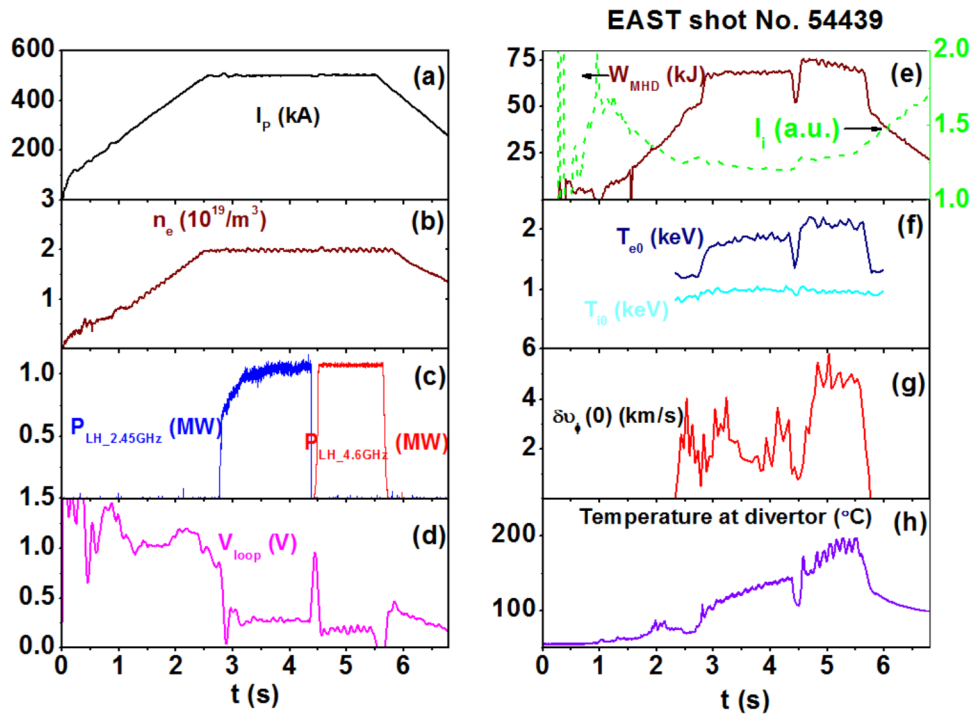


**Figure 3.** Typical waveform of LH frequency effect on plasma characteristics in the EAST Tokamak. (a) Plasma current (kA) versus time (s), (b) line averaged density ( $10^{19} \text{ m}^{-3}$ ) versus time (s), (c) LH power (MW) at 2.45 GHz in blue and LH power (MW) in red at 4.6 GHz versus time (s), (d) loop voltage (V) versus time (s), (e) stored energy (kJ) in brown and internal inductance (a.u.) in green versus time (s), (f) central electron temperature (keV) in blue and central ion temperature (keV) in cyan versus time (s), (g) central rotation velocity ( $\text{km s}^{-1}$ ) versus time (s), and (h) temperature at divertor ( $^{\circ}\text{C}$ ) versus time (s).

However, a transport analysis including LH CD sources would be needed in order to separate the contribution of heating and non-inductive CD to the loop voltage drop. One can gain insight into the effect of PI in the discharge shown in figure 5 by examining the behavior of the ECE as a function of density (see figure 6). Referring to figure 6 it can be seen that a weak power law is found ranging between  $n_e^{-1}$  and  $n_e^{-1.5}$ , suggesting a negligible behavior or weak effect from PI for the density range  $(1.5\text{--}5.0) \times 10^{19} \text{ m}^{-3}$  with the 4.6 GHz launcher.

In summary, experiments in EAST indicate that LHWs at 4.6 GHz exhibit stronger CD effect than at 2.45 GHz, possibly due to PI effect and the directivity of power spectrum. H-mode is obtained in EAST at relatively high density up to  $n_e \sim 4.5 \times 10^{19} \text{ m}^{-3}$  and further transport analysis is necessary.

## 2.2. Alcator C-Mod

On Alcator C-Mod, the LH RF physics program focuses on improving the CD at high density and understanding how to properly extrapolate present experiments to a reactor. The Alcator C-Mod device operates at high toroidal magnetic field strength (5–8 T) and high LH source frequency (4.6 GHz) which makes it possible to investigate LHCD physics at ITER relevant densities ( $\approx 0.7\text{--}1.0 \times 10^{20} \text{ m}^{-3}$ ) and although the pulse length is limited it is still possible to access discharges which are on the order of the ‘L/R’ or current relaxation time in the device. The power deposition of LH RF waves into the edge plasma of a diverted tokamak has been systematically measured for the first time in the experiment. By means of

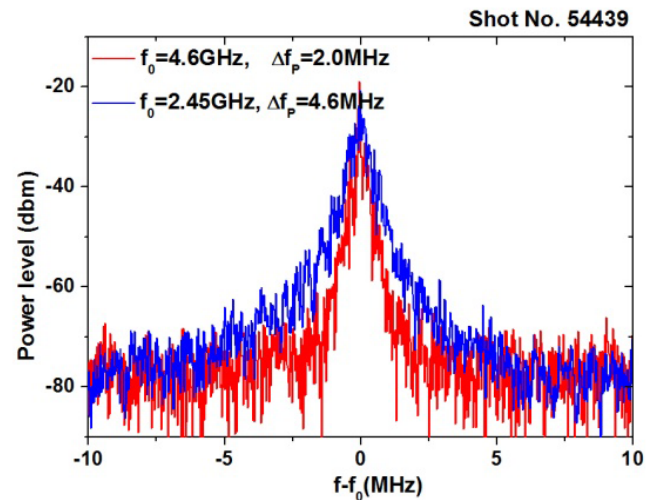


**Figure 4.** PI signal detected by an RF probe during 2.45 GHz (blue) and 4.6 GHz (red) LH power injection for in EAST. Reproduced courtesy of IAEA. Figure from [18]. Copyright 2017 IAEA.

fast time resolution edge diagnostic sets including innovative fast-thermocouples, an extensive set of Langmuir probes, and a Ly-alpha ionization camera, LH power modulation reveals that the LH power is deposited very close to or outside of the LCFS. The loss of CD at high density correlates with the existence of a cold, dense and highly collisional divertor plasma [20].

In a reactor, LH waves will experience strong single pass absorption, and therefore, the direct interaction with cold dense regions of the scrape-off-layer discussed above can be

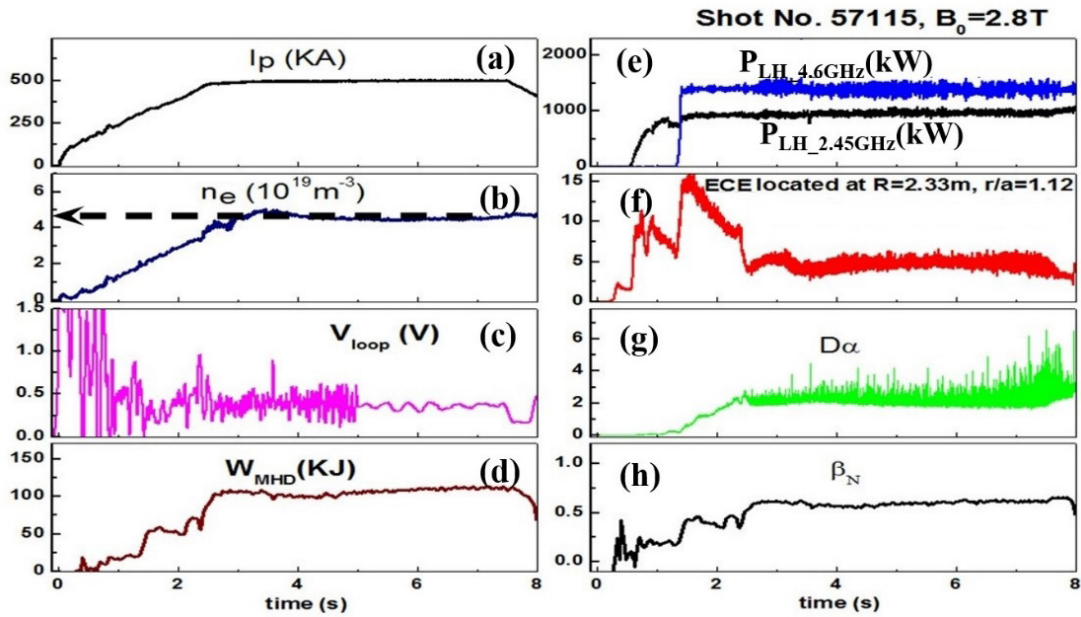


**Figure 5.** H-mode achieved with LHCD at high density in the EAST tokamak. (a) Plasma current (kA) versus time (s), (b) line averaged density ( $10^{19} \text{ m}^{-3}$ ) versus time (s), (c) loop voltage (V) versus time (s), (d) plasma stored energy (kJ) versus time (s), (e) 2.45 GHz LH power (MW) in black and 4.6 GHz power in blue versus time (s), (f) ECE versus time (s), (g)  $D\alpha$  emission versus time (s), and (h)  $\beta_N = \beta_t/[I_p(A)/(a(m)/B(T))]$  versus time (s). Reproduced courtesy of IAEA. Figure from [18]. Copyright 2017 IAEA.

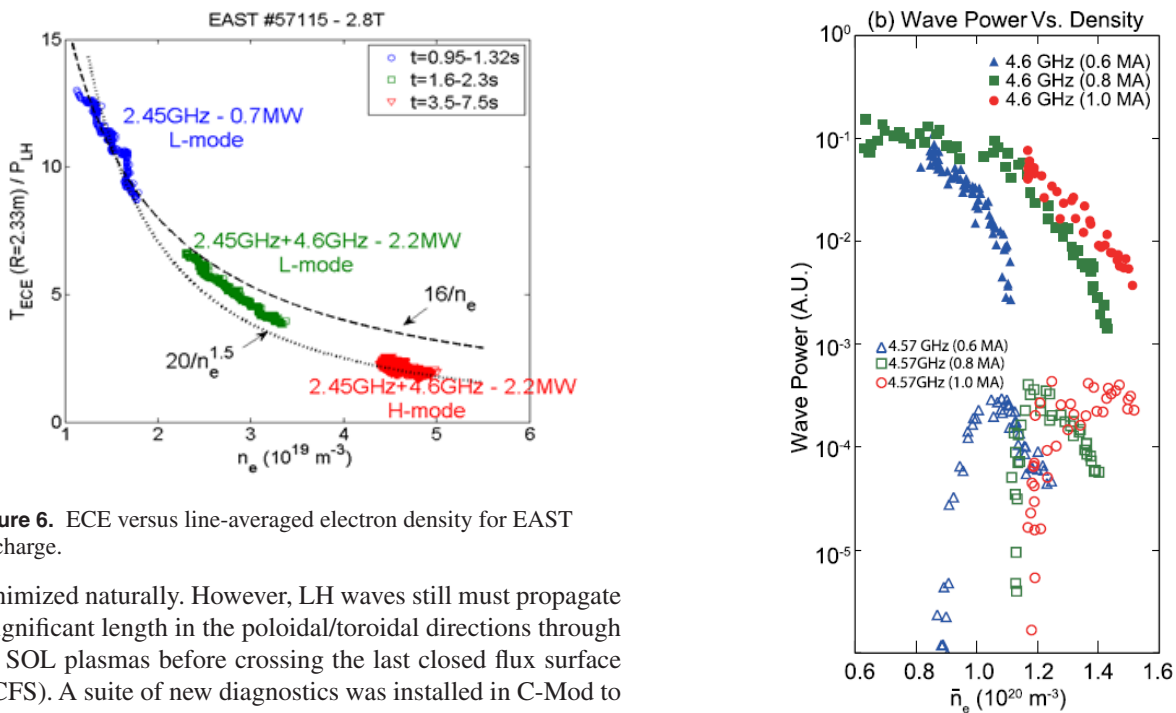


**Figure 6.** ECE versus line-averaged electron density for EAST discharge.

minimized naturally. However, LH waves still must propagate a significant length in the poloidal/toroidal directions through the SOL plasmas before crossing the last closed flux surface (LCFS). A suite of new diagnostics was installed in C-Mod to better characterize the LH wave propagation during this first pass from the launcher to core. Two sets of RF magnetic probe arrays were installed at different toroidal locations which are magnetically mapped to the launcher.

Figure 7 shows the LH wave power as a function of density measured by one of new RF probe arrays [13]. A reduction of LH power at the launched frequency (4.6 GHz) is observed in all three discharges with different plasma currents. The highest current case shows smaller reduction of LH power compared to other two. This trend is consistent with the recovery of CD at high current [21, 22], suggesting that significant

**Figure 7.** Wave power measured with the three probe array as a function of the line-averaged density at three different plasma currents in alcator C-Mod. Blue triangles, green squares, and red circles correspond respectively to 0.6 MA, 0.8 MA, and 1.0 MA discharges. Reprinted from [13], with the permission of AIP Publishing.

modification of the wave spectrum occurs during the first pass and may be responsible for the loss of CD. As the current is increased, the SOL width is measured to decrease significantly, placing the LH slow wave cut-off closer to the LCFS. This is consistent with reduced parasitic losses in the SOL

via CA (a reduction in the mean collisionality of plasma in the SOL) and PI, since now the distance transited by the LH wave between the cut-off and LCFS is reduced. Figure 7 also shows the signal strength at 4.57 GHz, indicating the spectrum power in this frequency range increases to about 10 dB below the peak power as the density increases. Note that the 4.57 GHz data shown in the figure corresponds to the ion-cyclotron PI sideband LH waves. In contrast to ion-sound PI's, which are stabilized with CA [23], those decay waves corresponding to the ion-cyclotron side bands remain unstable for a wide range of edge parameters found in various tokamaks and can be responsible for increased parasitic power losses universally observed in various LH experiments.

In summary, the C-Mod experiment at high density reveals that the injected LH power is deposited close to the LCFS, correlated with the existence of a cold, dense SOL plasma. With a reduction in the SOL width by increasing plasma current, the parasitic absorption during the first pass was reduced and the LHCD efficiency is found to be recovered to the level measured at a low density [21, 22].

### 2.3. JET

LHCD experiments in the JET device are carried out in a regime that is intermediate to that of EAST and Alcator C-Mod and overlaps with EAST where the magnetic field strength is 2–3 T, RF source frequency of 3.7 GHz and density in the range of  $2\text{--}4 \times 10^{20} \text{ m}^{-3}$ . Furthermore these experiments can be carried out in a regime that simultaneously tests both LH wave accessibility and conditions for parametric decay instability. The large complement of auxiliary NBI heating power in JET also makes it possible to test these effects under conditions where the LHRF power absorption is far off-axis (at  $r/a > 0.5$ ). On JET, for plasmas in weakly accessible conditions, the fast electron tail decays when the density is normalized to  $n_{e\text{-accessibility}}$  [24]. However the role of LH wave accessibility is difficult to assess when comparing the HXR (hard x-ray) data of EAST with 2.45 GHz system to the non-thermal ECE data of JET (see figure 8, where  $ECE_{\text{non th. JET}}$  means non-thermal ECE data in JET, HXR-EAST refers to HXR data in EAST, and the dash line represents the curve scaling with the density of  $n_e^{-8}$ ). A similar decay of the fast electron tail is observed for  $n_e > 2 \times 10^{19} \text{ m}^{-3}$  although the LH waves could penetrate deeper in the EAST plasma. Thus LH wave accessibility would not necessarily play a significant role in those discharges as indicated by similar behavior of fast electron data in inaccessible/accessible conditions [25, 26]. As will be discussed in section 3.4, recent time dependent RT/Fokker Planck analysis [27] has indicated that loss of wave accessibility at high density in JET could be partially responsible for a reduction in the LHCD effect. However this analysis relies on multiple passes of the LH wavefront between the slow wave cut-off and the confluence layer between the slow and fast wave modes in plasma. On the other hand, detailed analysis of spectral broadening via the PI effect has shown that this mechanism is a strong candidate for the decrease in HXR emission since the density at large radii in these discharges exceeds a critical value of

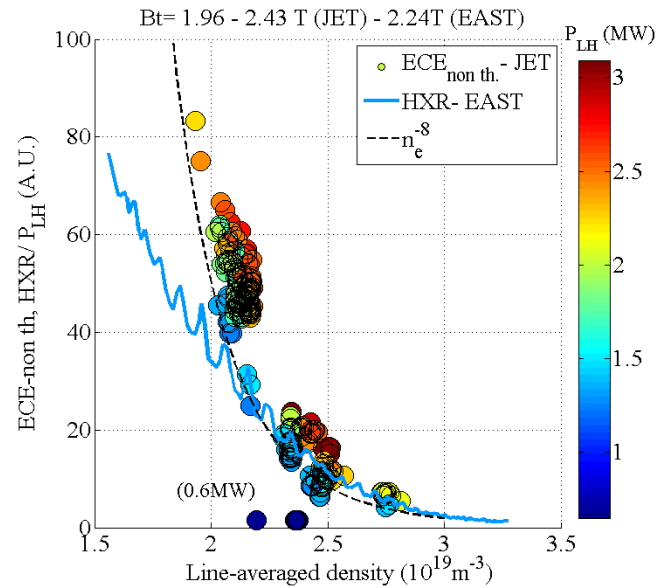


**Figure 8.**  $ECE_{\text{non th. (JET)}}$  and HXR (EAST) as a function of line-averaged density.

$\approx 4 \times 10^{19} \text{ m}^{-3}$ , which promotes conditions of cold plasma edge that favours the undesired effect of PI spectral broadening [7, 25]. Furthermore the experimental interpretation in terms of the PI effect can be understood in terms of a relatively straightforward single pass damping analysis.

### 3. Cross-study and data analysis

As can be seen from section 2, the C-Mod, EAST, and JET experimental devices provide a more or less continuous spectrum of plasma density, toroidal magnetic field strength, and RF source frequency for testing important aspects of LH wave physics. In this section we present modelling results for LHCD in C-Mod, EAST, and JET in order to elucidate the roles of LH wave accessibility, PI, CA, and SDF in determining wave absorption in these experiments as well as the larger decrease of CD efficiency than predicted by theory at high density [28]. In section 3.1 it will be shown through RT/Fokker Planck analysis of discharges in C-Mod and EAST that spectral broadening of the initial LH launcher spectrum (via processes such as PI and SDF) can be invoked in order to obtain profiles of LHRF power deposition, LH current density, and hard x-ray emission that are consistent with experimental measurements in these devices. In section 3.2 RT/Fokker Planck results are shown for Alcator C-Mod which demonstrates that CA of LH waves in the SOL can explain the reduction in hard x-ray emission as the density is increased. In section 3.3 a new RT/Fokker Planck model is applied to LHCD in JET where the role of LH wave accessibility at high density is assessed. Finally in section 3.4, analysis results are presented to interpret the differences seen in the LHCD efficiency with 2.45 GHz and 4.6 GHz LH power in EAST. In section 3.4.1 it is shown that suppression of PI at higher LH source frequency is also consistent with experimental results in the EAST experiments. Sections 3.4.2 and 3.4.3 assesses these experiments using RT/Fokker Planck treatments combined with a

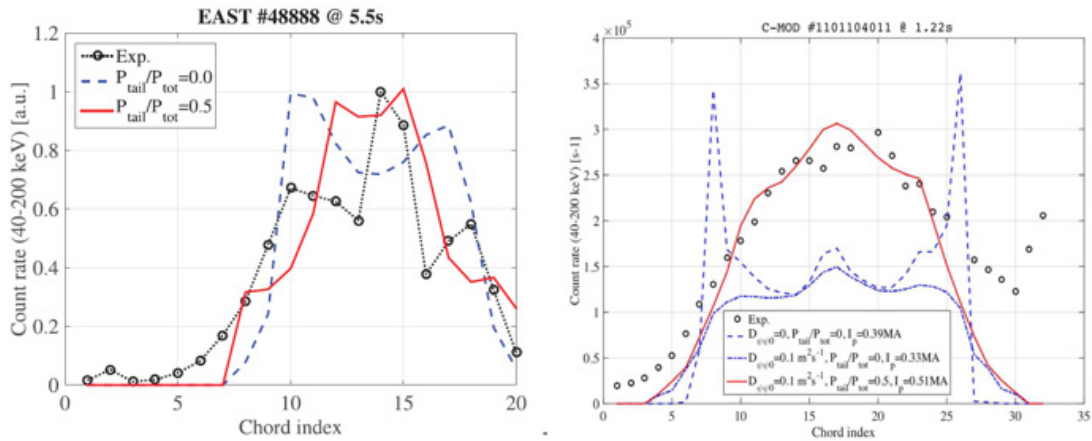


**Figure 9.** Comparison between experiment and calculation (C3PO/LUKE) with and without spectrum broadening (left: EAST, right: Alcator C-Mod). Reproduced from [29]. © IOP Publishing Ltd. All rights reserved.

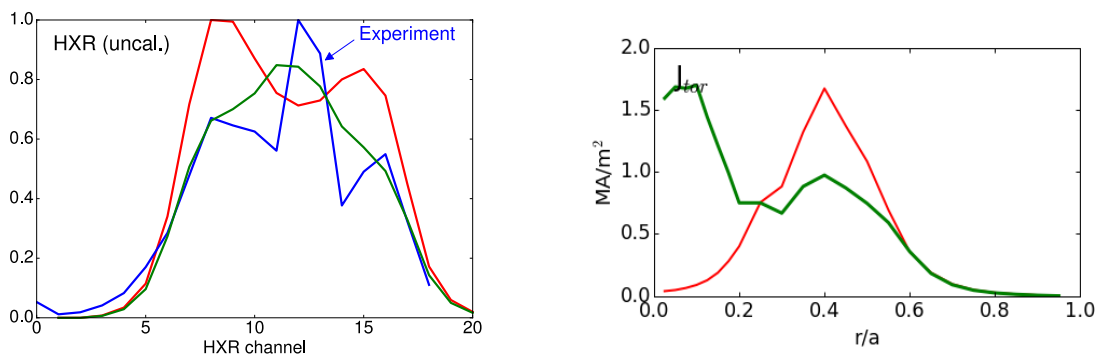


**Figure 10.** Comparison of HXR emission profile and current profile prediction (GENRAY/CQL3D), experiment (blue), simulation with (green) and without (red) spectral spreading (EAST #48888 at 5.5 s).

careful accounting for the coupled power spectrum from each frequency launcher. Section 3.4.4 concludes with a discussion of the difficulties associated with accounting for the DC electric field in these two-frequency discharges.

Simulations are based principally on two set of ray-tracing/Fokker–Planck (FP) codes, namely GENRAY/CQL3D and C3PO/LUKE. Comparisons between the two sets of codes have been done extensively in [29, 51] for LHCD. Both are describing the same physics, but their respective use is generally different, in particular the number of rays in the simulations, which may lead to significant differences when quasilinear effects become important. While GENRAY describes ray trajectory in the scrape-off layer, this feature is intentionally not considered in C3PO [29, 30, 51].

### 3.1. Role of spectral broadening in LHCD experiments in C-Mod and EAST

Measurements indicate there is little change in the LH power density profile in the density range where good CD is obtained. Furthermore, the simulated profiles of driven current density, power deposition, and hard x-ray emission do not always agree with experimental measurements in Alcator C-Mod [31] and TS [32], with the simulated profiles being off-axis, hollow, and sensitive to variations in plasma density compared to those in the experiment. The existence of a ‘tail’ in the launched power spectrum due to SDF [14], considered

in C3PO/LUKE codes [30, 33], greatly reduces model sensitivity to plasma conditions while at the same time significantly improves the consistency between modeling and experiments in plasma conditions for which the spectral gap is large in EAST and Alcator C-Mod [29], as well as in the TS tokamak (see figure 9). The spectral modifications employed in C3PO/LUKE typically place  $\leq 50\%$  of the incident LH power in a ‘tail’ that extends from  $2 \leq N_{||} \leq 5$  and that is modeled by a series of smaller Gaussian power lobes.

The ‘tail’ model employed in GENRAY/CQL3D [34, 35] places 5%–10% of the incident LH power in smaller Gaussian power lobes at  $N_{||} \approx 2.5$ –2.7. An example using GENRAY/CQL3D for the EAST tokamak is shown in figure 10, where a relocation of 10% of total LH power to modestly high  $N_{||}$  ( $\sim 2.7$ ) gives the best fit to the experimental HXR emission profile shape. At this time the differences needed in the spectral broadening in C3PO/LUKE and GENRAY/CQL3D in order to improve agreement with experiment are under study. Regardless, the introduction of spectral broadening in the injected LH wave power spectrum, attributed to physical effects such as wave scattering from density fluctuations or parametric decay instability, can be seen to be an important feature to include when interpreting LHCD experiments.

The whole consistency between toroidal MHD equilibrium and ray-tracing/FP LH current density profile in presence of a non-zero residual loop voltage or if the current density is not expected to have relaxed towards its steady-state or

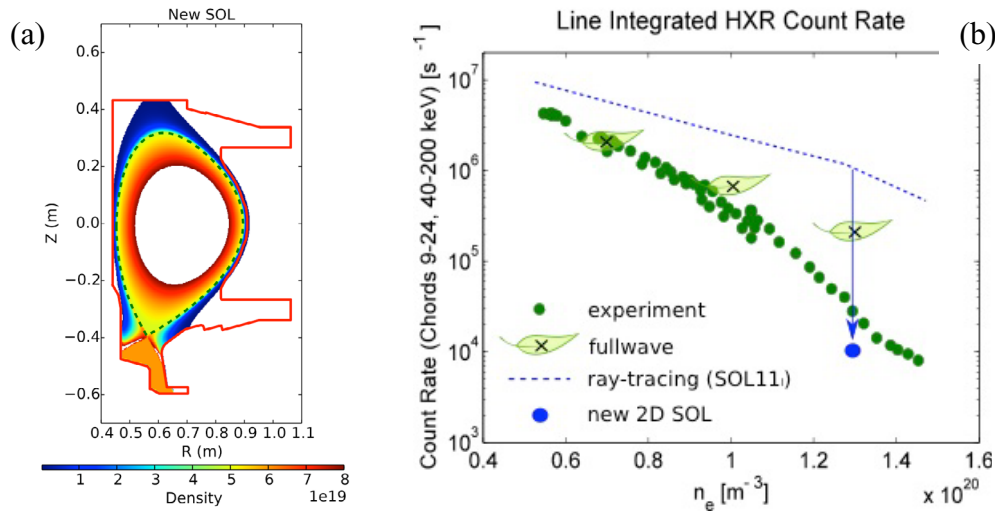


**Figure 11.** (a) New SOL model employed in GENRAY. (b) GENRAY/CQL3D prediction of HXR emission intensity when 2D realistic SOL is used (blue). Also shown are the experimental HXR count rates in green, the simulated HXR count rates using the simplified SOL model (SOL11) in GENRAY, and the HXR counts predicted by the LHEAF full-wave LH solver which includes a simplified SOL.

stationary is necessary. For Alcator C-Mod case, the role of the residual Ohmic parallel electric field is found marginal, and the fact that the predicted LH current has a shape close to toroidal MHD indicates that the ray-tracing/FP solution is already close to the self-consistent one. For the EAST case, this is a full CD discharge for which the steady-state regime was achieved [29]. In both cases, the ‘tail’ in the launched power spectrum has led to obtain LH current density profiles close to the target toroidal MHD equilibrium, thus reducing the importance of the self-consistency procedure.

### 3.2. Role of CA in the alcator C-Mod density limit

LHCD experiments on C-Mod, EAST, and JET are generally carried out in regimes where electron Landau damping is weak and the LH wavefront undergoes multiple reflections from cut-offs in the scrape off layer where collisional damping (CA) is important. Indeed simulations of CA using GENRAY/CQL3D suggest that SOL plasmas can have significant impact on CD when single pass absorption is weak. Recently a model which takes into account realistic SOL geometry and the existence of a cold dense plasma near the divertor was implemented in GENRAY. Previously when the computation domain of GENRAY had been extended to include SOL plasmas, the SOL plasma density and temperature profiles were assumed to be an exponential function, referred to as SOL11 in figure 11(b). Although the scalelength of the exponential function was selected to match the profile measured at the outboard mid-plane, it did not incorporate the actual SOL plasma geometry, such as the divertor X-point. In order to investigate the importance of SOL geometry, a new SOL model was incorporated into GENRAY/CQL3D [36]. The model uses a measurement of  $T_e$  and  $n_e$  on the midplane and  $T_e$  on the divertor tiles (the so-called ‘two point model’), and computes the density and temperature elsewhere along the field line based on pressure conservation along the field line and classical Spitzer parallel heat conduction. As shown

in figure 11(a), the new SOL profile is significantly different near the divertor region. This improved model for the SOL predicts a more significant reduction of CD as the density is increased compared to previous work [37] and is more consistent with experiment [36] (see figure 11(b)).

### 3.3. RT/Fokker Planck analysis of JET discharges at high density

In JET, a series of LH power modulation experiments were carried out which provides unique data for validating the LHRF power deposition profiles predicted by RT/Fokker Planck models. Notably this type of data is not available from LHCD experiments on EAST or Alcator C-Mod, yet. A new RT/FP package (JRT), with a real 2D geometry accounting for the plasma boundary and launcher shape and a new 3D relativistic bounce averaged FP code, has been developed [38] for LH power deposition analysis and the main results are shown in figure 12. Power deposition profiles from the code are compared to experimentally assessed profiles from modulated LH experiments [39] and ECE analysis data [40]. Calculations are in a reasonable agreement with experimental data at low density (discharge #77609,  $n_e \approx 2.4 \times 10^{19} \text{ m}^{-3}$ ) and high density (discharge #77612,  $n_e \approx 3 \times 10^{19} \text{ m}^{-3}$ ). The code cannot reproduce absorption at the cold periphery ( $0.6 < \rho < 0.8$ ) in both cases whereas in addition to this at high density (#77612) the calculated core absorption ( $\rho < 0.2$ ) is much higher than experimental results. Simulations with broadened initial  $N_{||}$  spectra (i.e. upshift of  $N_{||}$  up to 2.5) resulted in more consistent deposition in the periphery with numerical results matching experimental data up to  $\rho \approx 0.7$ .

The broadening of the initial  $N_{||}$  spectra in the simulations shown in figure 12 has been studied by examining the evolution of the rays and statistically analysing the changes in rays’  $N_{||}$  during their propagation in plasma. Figure 13 shows the evolution of a typical ray, launched close to the mid-plane,  $Z_0 = 0.22 \text{ m}$  with  $N_{||} = 1.82$ , which is representative

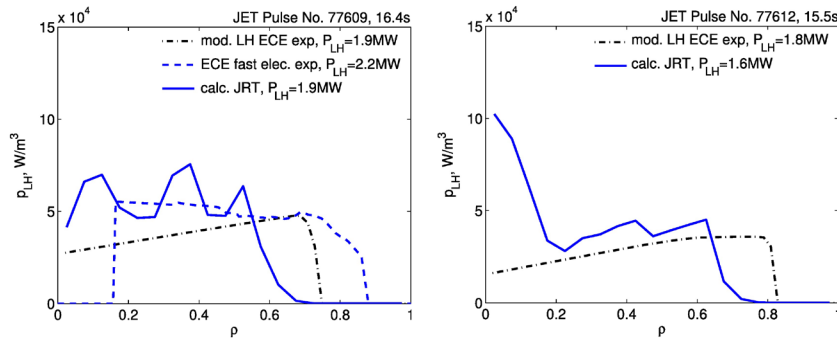


**Figure 12.** LH wave power deposition profiles of JET for 3.4 T/1.5 MA, line averaged  $n_e = 2.4 \times 10^{19} \text{ m}^{-3}$ , central  $T_{e0} = 3 \text{ keV}$ , low density pulse #77609 (left figure) and for 3.4 T/1.8 MA, line averaged  $n_e = 3.0 \times 10^{19} \text{ m}^{-3}$ , central  $T_{e0} = 3.5 \text{ keV}$ , high density pulse #77612 (right figure). The power deposition profiles, provided by JRT code,  $P_{LH}$  (solid blue lines), were calculated with real  $N_{||}$  spectra of the launched waves. The experimental profiles provided for comparison were determined from LH modulation experiments (dash-dotted black lines) [39] and alternatively from the ECE analysis of the supra-thermal electrons (dashed blue line) [40]. The total amount of experimentally assessed and calculated absorbed power,  $P_{LH}$ , in shown in the legends for all cases.

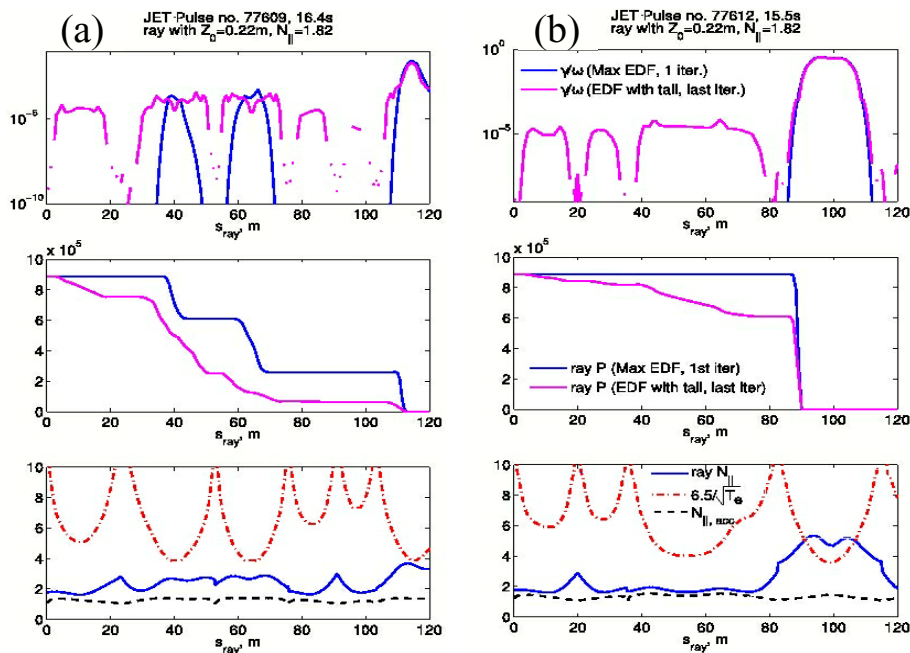


**Figure 13.** Ray parameters evolution versus ray path  $s_{ray}$  for low density (a) and high density (b) JET pulses #77609 and #77612. Top two graphs show the rays absorption  $\gamma/\omega$  and ray's power  $P$  calculated with Maxwellian EDF corresponding to the first WS–FP iteration (blue lines) and with fully evolved EDF with quasilinear plateau corresponding to the last (14th) WS–FP iteration (magenta). The bottom graphs show ray's  $N_{||}$  (blue line), the value of  $N_{||}$  at which strong Landau damping occurs at  $6.5/\sqrt{T_e} \equiv 6.5/(T_e)^{1/2}$  (red dash-dotted line) and the accessibility  $N_{||,acc}$  (black dashed line) at the ray's position.

of the maximum power spectrum. The absorption of the ray, i.e. the value of  $\gamma/\omega$ , and its attenuation are shown in the top two graphs for the first iteration (blue lines) between wave solver (WS) and FP code, in which case Maxwellian electron distribution function (EDF) is assumed and the final iteration (magenta lines) in which case fully evolved EDF with plateau is used in the  $\gamma/\omega$  calculation. In the bottom graph ray's  $N_{||}$  is provided together with the accessibility at the ray position,  $N_{||,acc}$ , and the values of  $N_{||}$  where good absorption is expected, which has been assessed to be at  $6.5/(T_e)^{1/2}$ .

Clearly in the low density case, JET pulse #77609 in figure 13(a), with wave power absorption calculated after the first WS–FP iteration (blue lines), an upshift in  $N_{||}$  is required for the ray power to be fully absorbed, which happens for  $N_{||} \sim 2.7$  ( $s_{ray}$

$\sim 40 \text{ m}$  and  $s_{ray} \sim 65 \text{ m}$ ) near the local minima of the quantity  $6.5/(T_e)^{1/2}$ , estimated to be about 3.8. After the last WS–FP iteration EDF is fully evolved, with a quasilinear plateau. This allows ray's power absorption to happen for lower  $N_{||}$  as seen from the magenta lines in figure 13(a). The bottom graph shows that with fully evolved EDF ray absorption occurs in a wider range around local  $6.5/(T_e)^{1/2}$  minima, implying larger difference between  $6.5/(T_e)^{1/2}$  and  $N_{||}$  in the absorption zone. In this example the ray stays well above its local accessibility refractive index,  $N_{||,acc}$ , as shown in the bottom graph and never mode-converts to fast wave. Nearly all of the LH slow wave power,  $\sim 86\%$ , is absorbed before first mode conversion of the rays.

It is important to note the central electron temperature was comparable in these two cases despite the difference

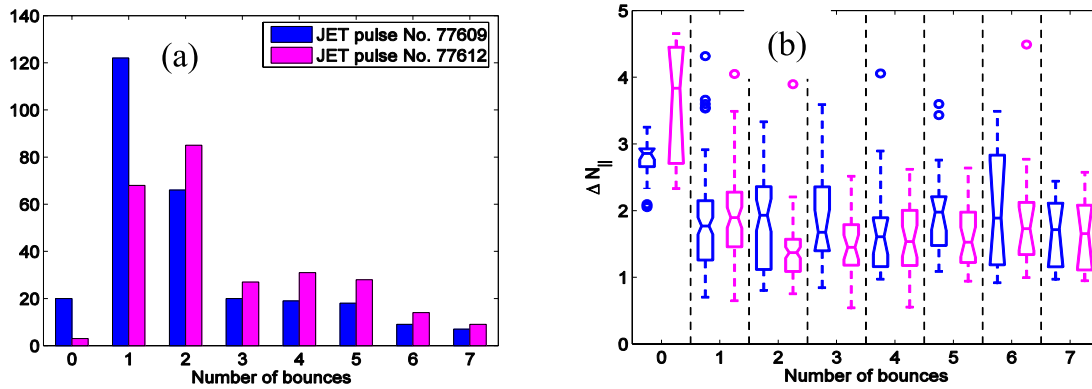


**Figure 14.** Statistical analysis of rays' parameters evolution versus number of bounces off plasma boundary for JET pulses #77609 (blue) and #77612 (magenta). Histograms of the number of rays versus number of bounces before maximum absorption occurs is shown in (a). Boxplot statistics of rays' parallel refractive index upshift,  $\Delta N_{||} = 6.5/\sqrt{T_e} - N_{||}$ , versus the number of bounces before rays reaches maximum attenuation, i.e. *maximum of ray's power drop*, is shown in (b).

in density. In the low density discharge the central electron temperature was of the order of  $T_{e0} \approx 3$  keV, i.e. a relatively cold plasma in L-mode with a small amount ( $< 1.4$  MW) of NBI power for diagnostic purposes. In the higher density case with H-mode like density pedestal a higher central electron temperature  $T_{e0} \approx 3.5$  keV was achieved by applying  $\sim 9.5$  MW of NBI power.

In the high density case, JET pulse #77612, figure 13(b), the ray requires significant  $N_{||}$  upshift for the ray's power to be fully absorbed. This happens at  $s_{\text{ray}} \sim 90$  m for  $N_{||} \sim 4.6$ , which value is again close to the local minimum of  $6.5/(T_e)^{1/2} \sim 5.5$ . Using the fully evolved EDF as provided after the last WS-FP iteration allows some ray power absorption to happen for lower  $N_{||}$  (see figure 13(b) magenta) but a considerable amount of power remains until  $N_{||}$  upshifts again to about 4.6 where it is eventually absorbed. The difference in  $N_{||}$  at which LH wave power is absorbed in the two cases,  $\sim 2.7$  for #77609 and  $\sim 4.6$  in #77612, is considerable in terms of velocity of the resonant electrons, which scales as  $c/N_{||}$ . For most of its propagation the ray stays close to  $N_{||,\text{acc}}$ , but it mode-converts to fast wave at the very end,  $s_{\text{ray}} > 120$  m (not shown in the graph), after all power is fully absorbed. About half of the LH slow wave power,  $\sim 48\%$ , is absorbed before first mode conversion of the rays.

Statistical analysis, figure 14, of all 288 rays used in both calculations supports the conclusions stated above. Results shown in figure 14 are for the case with fully evolved EDF as provided by the last WS-FP iteration. As shown in figure 14(a), histograms most of the rays need 1–2 bounces before experiencing maximum absorption. For pulse #77609 significantly more rays are absorbed after just one bounce, figure 14(a), while at high density pulse #77612 the number of rays requiring 2–5 bounces to reach maximum absorption is much higher meaning higher probability of  $N_{||}$  upshift. In figure 14(b) the number of rays' bounces before maximum absorption of the rays occur is analysed versus rays'  $N_{||}$  evolution. As a measure of the latter we use the difference  $\Delta N_{||} = 6.5/(T_e)^{1/2} - N_{||}$  at the location of the maximum rays' absorption. In the lower density case #77609 (blue lines in figure 14(b)) the  $\Delta N_{||}$  averaged over all rays is about 1.9, while for #77612 (magenta lines in figure 14(b)) this number drops to 1.6. For rays

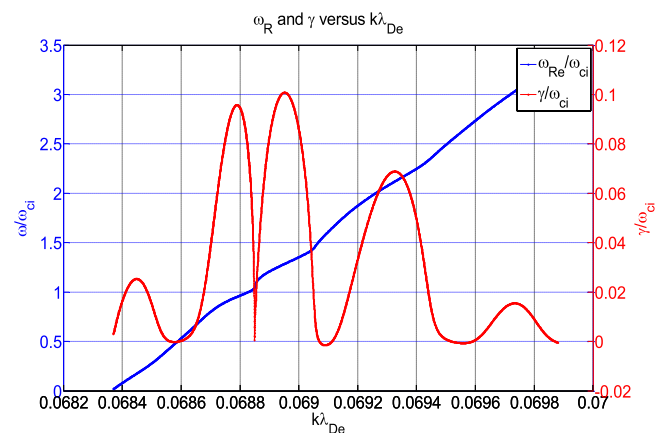


**Figure 15.** Growth rate calculation for pump frequency  $f_0 = 2.45$  GHz,  $n_e = 3 \times 10^{18} \text{ m}^{-3}$ ,  $T_e = T_i = 50$  eV,  $B = 2.8$  T,  $ck_{||0}/\omega_0 = 2.1$  (pump wave),  $ck_{||}/\omega_0 = 7$  (sideband),  $P = 3.2$  MW  $\text{m}^{-2}$ .

requiring two or more bounces the difference  $\Delta N_{||}$  is lower for high density cases meaning that higher  $N_{||}$  upshift in this case. Interestingly, for rays requiring just one bounce off the plasma boundary before reaching maximum absorption the averaged  $\Delta N_{||}$  values are approximately the same,  $\sim 1.8$ , in both cases.

To summarise, one can conclude that indeed the initial  $N_{||}$  spectrum upshifts during rays' propagation and this is better pronounced at higher densities, where in general rays bounce more before being absorbed. In addition, at higher density the effect of  $N_{||}$  upshift is better pronounced as rays' power is absorbed for lower  $\Delta N_{||}$ , i.e. closer to the local value of  $6.5/(T_e)^{1/2}$  compared to the low density case.

#### 3.4. Investigation of the difference in two-frequency LHCD in EAST

**3.4.1. Analysis of PI in two-frequency LHCD discharge in EAST.** Previous experiments on FTU indicated that SDF would not play a significant role in tokamak experiments performed so far at high plasma densities, since LHCD effects (as inferred from hard x-ray emission) occurred at very high density ( $n_e = 2 \times 10^{20} \text{ m}^{-3}$ , with ITER-relevant  $n_e$  profile and high  $T_e$  periphery regime) in the presence of a RF probe

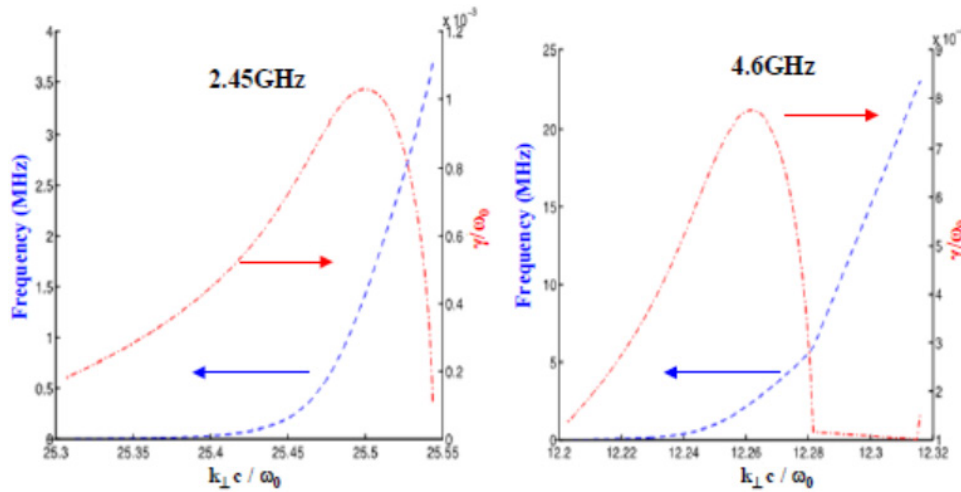


**Figure 16.** Frequencies (blue dash lines) and growth rates (red dot-dash lines) versus  $k_{\perp} c / \omega_0$  calculated by the LHPI code for parameters characteristic of the middle of the SOL in EAST ( $r/a \approx 1.01$ ,  $n_e = 4 \times 10^{18} \text{ m}^{-3}$ ,  $T_{ea} = T_{ia} = 10 \text{ eV}$ ). (left: 2.45 GHz, right: 4.6 GHz).

spectrum that was symmetrically broadened (up to 7 MHz), attributable to SDF [7]. Conversely, a significantly broadened and downshifted spectrum (up to 15 MHz), not accompanied by any LHCD effect in plasma was produced in standard high-density regime, consistent with PI modelling results [7]. Based partly on the FTU results we are thus motivated to analyze the possible role of PI in the EAST two-frequency discharge.

Modeling of PI using the LHPI code [41] and a growth-rate solver [42, 43] originally based on the parametric dispersion relation derived by Porkolab [44], that has been extended [43] to include another form of the dispersion following the approach in Liu [45], are qualitatively consistent with the measured RF spectrum. Using this solver, recent investigations have focused on the parametric excitation of the LH wave (sideband) in the parallel coupling limit. In this limit, the excited sideband LH wave can propagate nearly along the launched LH pump wave. Since the sideband can be excited and its amplitude can grow only in the presence of the pump, this parallel coupling case could result in a higher sideband amplitude in high density plasmas for which the pump wave has a limited radial penetration and spends longer time at the plasma edge where it is unstable to parametric instabilities. Figure 15 shows an example of the normalized frequency ( $\omega_R/\omega_{ci}$ ) and growth rate ( $\gamma/\omega_{ci}$ ) spectra when  $\theta = 10^\circ$  in EAST. In this particular case, one interesting feature is the appearance of a dip in the growth rate spectrum around the ion cyclotron first-harmonic solution ( $k\lambda_{DE} \approx 0.06883$ ). This dip is due to the upper sideband also being nearly resonant ( $\epsilon^+ \approx 0$ ), which is generally off-resonant and does not contribute much in determining  $\gamma$  in the limit  $\theta \rightarrow 90^\circ$ .

Based on the experiments in section 2.1, the effect of LH frequency (2.45 GHz and 4.60 GHz) on PI in EAST has been analysed. Considering the typical EAST plasma with a line-averaged plasma density of  $2 \times 10^{19} \text{ m}^{-3}$  and using the LHPI code, the calculated frequencies and growth rates of PI driven mode are shown in figure 16, in which the RF coupled power of 1 MW, the antenna power spectrum peak ( $N_{j0} = 2.0$ ) and the EAST antenna dimensions have been considered. For the pump frequency of 4.60 GHz, the analysis performed by the

LHPI code shows that the PI mechanism is mostly driven by a low frequency quasi-mode in the range of ion-sound evanescent modes (of about 2 MHz), consistent with the observed phenomenon of spectral broadening. Assuming kinetic radial profiles merging the available data of the SOL and main plasma, for the case of 2.45 GHz, the normalised maximum homogeneous growth rate in the middle of the SOL (at  $r/a \approx 1.01$ ,  $n_e = 4 \times 10^{18} \text{ m}^{-3}$ ,  $T_{ea} = T_{ia} = 10 \text{ eV}$ ) reduces from  $\gamma/\omega_0 \approx 1 \times 10^{-3}$  (see figure 16) by about a factor two at  $r/a \approx 0.8$ , and is still positive at  $r/a \approx 0.5$ . In contrast, for 4.60 GHz, the corresponding value in the middle SOL is smaller (by about 20%, see figure 16), reduces by about a factor of three at  $r/a \approx 0.8$ , and the plasma becomes stable (i.e. the growth rate is negative) for  $r/a < 0.7$ . Since PI occurrence is regulated by convective losses [41, 45], these results suggest that the phenomenon should be less pronounced for the case of 4.60 GHz, because the wave group velocity is higher at higher frequency, resulting in the wave staying in the convective growth region for less time.

Calculations with the parametric dispersion code described in [42, 43] at frequencies of the PI driving mode near the first ion cyclotron harmonic show that the growth rate is positive and finite for both 2.45 GHz and 4.6 GHz but reduces by a half at 4.6 GHz (see figure 17). Additionally a scan was done of power density for each of the LH grill launchers which suggests that PI instability will occur even down to the lowest power density examined as can be seen in figure 17. For each frequency case examined the actual grill area was used corresponding to  $0.202 \text{ m}^2$  for the 2.45 GHz launcher and  $0.198 \text{ m}^2$  for the 4.6 GHz launcher while injected LH powers of (0.2, 0.4, 1.0) MW were used with each frequency. For each of the parametric dispersion calculations shown in figure 17 the electric field is found from the WKB approach and the perpendicular wavenumber of the lower sideband is assumed to be normal to the perpendicular wavenumber of the pump wave. Results for the computed growth rate at 0.4 MW are not shown in figure 17, although those growth rate values were found to lie between the 1.0 MW and 0.2 MW cases.

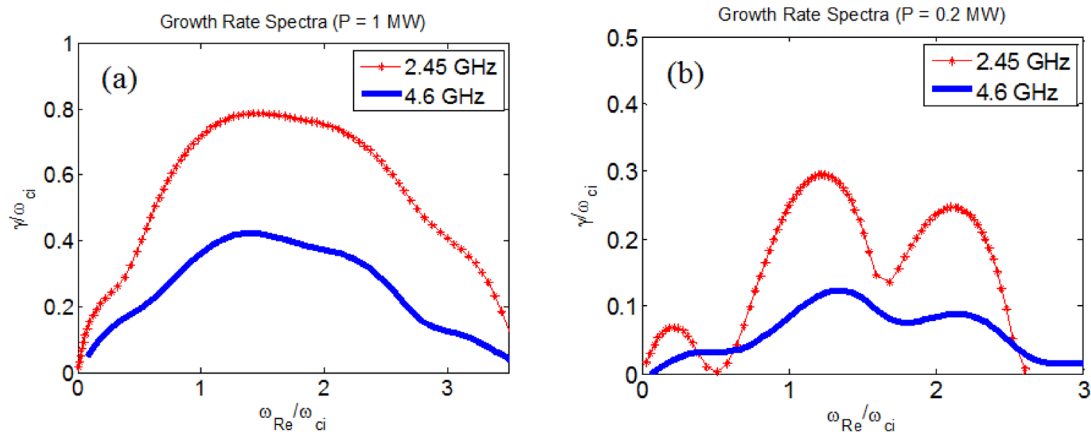


**Figure 17.** Computed growth rate spectra with  $f_0 = 2.45$  GHz (red asterisk) and 4.6 GHz (blue line) using the parametric dispersion code described in [42, 43]. The parameters assumed are deuterium plasma,  $n_e = 5 \times 10^{18} \text{ m}^{-3}$ ,  $T_e = T_i = 30 \text{ eV}$ ,  $B_t = 1.83 \text{ T}$ ,  $N_{||0} = 2$ , and the ion mode  $N_{||} = 7$ . (a) 1 MW injected LH power with  $P_{\text{RF}, 2.45 \text{ GHz}} = 4.95 \text{ MW m}^{-2}$  ( $=1 \text{ MW}/0.202 \text{ m}^2$ ) and  $P_{\text{RF}, 4.6 \text{ GHz}} = 5.05 \text{ MW m}^{-2}$  ( $=1 \text{ MW}/0.198 \text{ m}^2$ ). (b) 0.2 MW injected LH power with  $P_{\text{RF}, 2.45 \text{ GHz}} = 0.99 \text{ MW m}^{-2}$  ( $=0.2 \text{ MW}/0.202 \text{ m}^2$ ) and  $P_{\text{RF}, 4.6 \text{ GHz}} = 1.01 \text{ MW m}^{-2}$  ( $=0.2 \text{ MW}/0.198 \text{ m}^2$ ).

**3.4.2. Power spectrum analysis of two-frequency LHCD discharge in EAST.** The two-frequency LHCD experiment performed in EAST is based on the use of two different antennas, whose geometrical characteristics may have a direct impact on the coupled power spectra and the overall ray-tracing/FP simulations. It is therefore critically important to evaluate them carefully with a rigorous procedure, taking into account of the operating conditions at the times considered for the simulations. This is carried out with ALOHA coupling code running in 1D mode [15], using experimental input powers and phases of each module and for each row. The latter are accurately measured just in front the ceramic window. The density in front of each row is determined by minimizing the difference between calculated and measured reflected power levels in each module, keeping the density scale length to its default value  $\lambda = n/\nabla n = 0.02 \text{ m}$ , as calculations are rather weakly sensitive to this parameter. From EAST LH experiments, the low density solution of the RC is considered, since moving away antennas from the plasma separatrix leads systematically to a degradation of the coupling conditions. Once the density is self-consistently determined, the power spectrum is evaluated for each row, and the global power spectrum for the whole antenna is evaluated by summing over all antenna rows of waveguides. This procedure is preferred to the one considering direct measurements of the density by Langmuir probes. Indeed, the density may change significantly along the poloidal direction, and measurements are too sparse for an accurate determination of the power spectra, as required by calculations of the RCs. Nevertheless, the densities self-consistently determined from RCs for the 2.45 and 4.6 GHz antennas,  $1.0 \times 10^{17} \text{ m}^{-3}$  and  $5.0 \times 10^{17} \text{ m}^{-3}$  respectively, are found to be reasonably close to Langmuir measurements of the order of  $1.0 \times 10^{18} \text{ m}^{-3}$ , as shown for TS LH studies [46]. The input power spectra by ALOHA for antennas at 2.45 GHz and 4.6 GHz are shown in figures 18(a) and (b). Here, the spectrum is expressed as a function of the refractive index component along the toroidal direction (Fourier transform along this direction),  $N_z$ , since a simplified slab geometry

is assumed at the plasma edge near the grill without any poloidal dependence. As far as the safety factor is high enough near the separatrix,  $N_{||}$  may be reasonably approximated to  $N_z$ , since the poloidal field component is very small as compared to the toroidal one. However, when  $B_z/B_p$  is becoming significant, a correction must be considered, and  $N_{||} = N_z * B_z/B$ , where  $B_z$  and  $B_p$  are the toroidal and poloidal components of the magnetic field amplitude ( $B$ ), respectively.

Due to the rather large RCs for the 2.45 GHz antenna, reaching 10% approximately, multiple satellite lobes appear, either at high- $N_{||}$  in the co-current side ( $N_{||} < 0$ ) and counter-current side ( $N_{||} > 0$ ), leading to an overall degradation of the power in the main co-current lobe of the 2.45 GHz antenna, as compared to the antenna at 4.6 GHz where the power in the main co-current lobe is higher at same input power level.

**3.4.3. RT/Fokker analysis of two-frequency LHCD discharge in EAST.** From standard ray-tracing/FP calculations using C3PO/LUKE codes based on the power spectra determined as explained in the previous section, the LH-driven currents are estimated to be 85 kA at 4.15 s for the 2.45 GHz antenna and 94 kA at 5.15 s for the 4.6 GHz antenna [47]. Such a result is consistent with the larger loop voltage drop at 5.15 s, which indicates better CD efficiency when operating with the 4.6 GHz antenna. This result is obtained despite the larger measured effective charge,  $Z_{\text{eff}}$ , when using the 4.6 GHz antenna, which increases from 2.8 to 3.0 at the considered time slices. The non-resonant CA at the plasma edge is found negligible, therefore  $\sim 100\%$  of the LH power coupled to the plasma is absorbed by Landau resonant absorption in the calculations. As noted above, these simulations did not employ a ‘tail’ in the LH power spectra. Also fast electron transport was turned off in the Fokker Planck code (LUKE).

RT/Fokker Planck calculations using the GENRAY/CQL3D codes have also been carried out for the same plasma profiles, MHD equilibrium, and LH power spectra that were used in the C3PO/LUKE simulations of LHCD for the 2.45 GHz antenna at 4.15 s and the 4.6 GHz antenna at 5.15 s

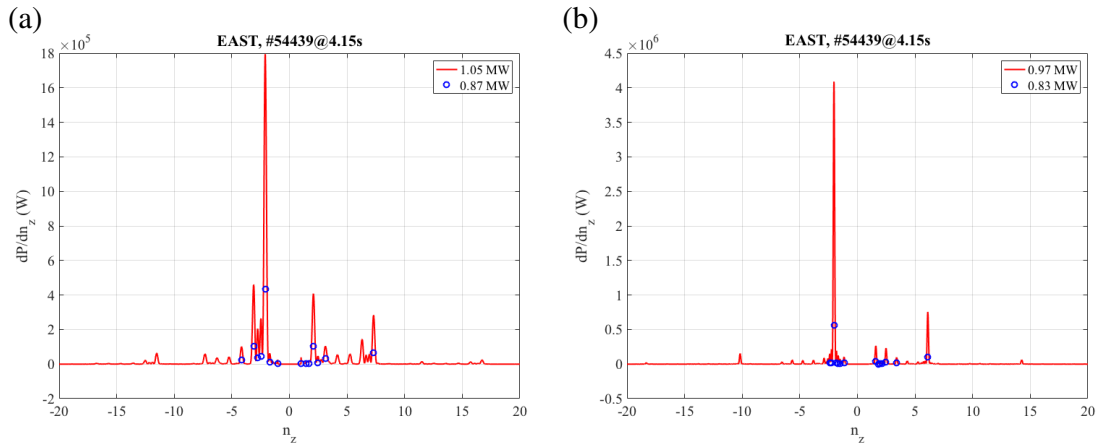


**Figure 18.** (a) Power spectrum for the 2.45 GHz antenna evaluated by ALOHA 1D code. The density in front of the antenna is about  $1.7 \times 10^{17} \text{ m}^{-3}$ . Blue circles correspond to the prominent lobes for CD considered for ray-tracing calculations. With 14 selected lobes, the effective power available for CD calculation is 0.87 MW, while power carried by all lobes is 1.05 MW. The lobe selection preserves antenna directivity. (b) Power spectrum for the 4.6 GHz antenna evaluated by ALOHA 1D code. The density in front of the antenna is about  $5 \times 10^{17} \text{ m}^{-3}$ . Blue circles correspond to the prominent lobes for CD considered for ray-tracing calculations. With 14 selected lobes, the effective power available for CD calculation is 0.83 MW, while power carried by all lobes is 0.97 MW. The lobe selection preserves antenna directivity.

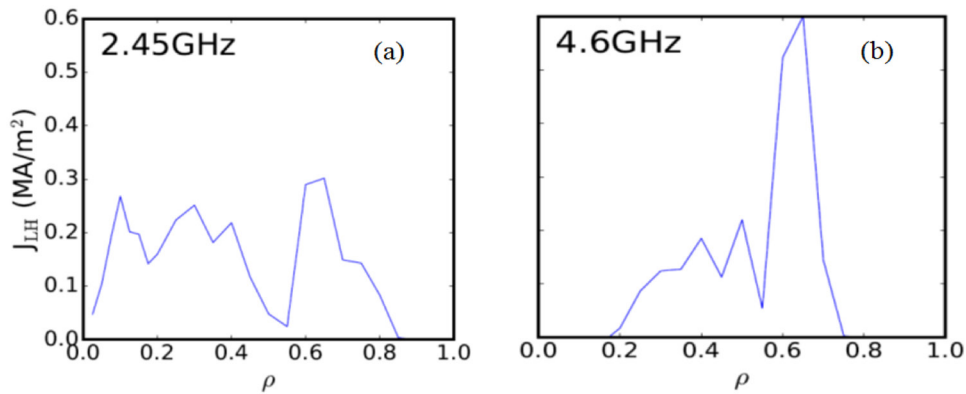


**Figure 19.** GENRAY/CQL3D simulations of LH CD in EAST using LH power spectra from the ALOHA code shown in figure 18 with zero DC electric field for the (a) 2.45 GHz antenna at 4.15 s and for the (b) 4.6 GHz antenna at 5.15 s. The total LH current in each case is  $\sim 130 \text{ kA}$ .

described above. The total driven LH current in the absence of the DC electric field was found to be about 130 kA in the case of each frequency with the 4.6 GHz current profile peaked farther off-axis than the 2.45 GHz as can be seen in figures 19(a) and (b).

Note that without loop voltages, but considering the same magnetic MHD equilibrium and initial ray conditions, GENRAY/CQL3D and C3PO/LUKE calculate different current density profiles for the two cases here considered, though some similarities are observed when the LH frequency is increased from 2.45 to 4.6 GHz. Indeed, power absorption is more central and broad for 2.45 GHz, while it is more off-axis at 4.6 GHz for both codes. The differences between predictions may result from several reasons, like the different number of rays used in the simulations, the spectral width for each ray, which may impact quasi-linear convergence. Despite accurate benchmarks and the excellent agreement between the two set of codes in the linear limit like for the LH wave in ITER [1], the very sensitive weak absorption regime here considered, may reveal some differences in their use [29, 51].

This is likely an indication of the limit of prediction of these numerical tools when conditions of applicability become marginal.

**3.4.4. Current prediction in presence of a residual Ohmic electric field.** With a residual Ohmic electric field corresponding to  $V_{\text{loop}} = 0.27 \text{ V}$  and  $V_{\text{loop}} = 0.15 \text{ V}$  at 4.15s and 5.15s respectively, while LH power is applied, synergistic effects must be considered to evaluate the total driven current.

In a preliminary study, the time evolution of the #54439 discharge is calculated with the METIS code [48], thus allowing to determine the global consistency between different measurements, using simple 1D fluid model. In this simulation, the loop voltage is determined to match the observed current level, while temperature is determined from transport calculations using prescribed density and  $Z_{\text{eff}}$  profiles.

As shown in figure 20, in the Ohmic phase after the current flat-top, the predicted loop voltage is more than twice the observed  $V_{\text{loop}}$  level, as well as the total energy content. This discrepancy, which lasts during all the discharge, including

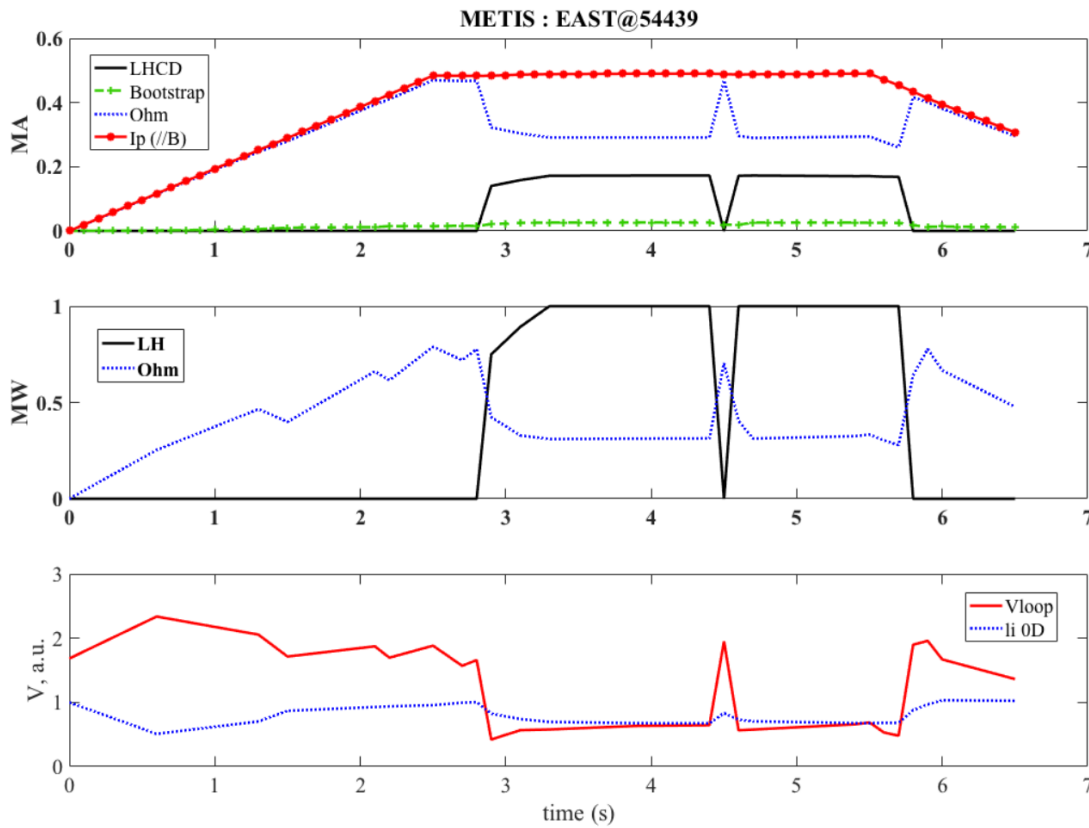


**Figure 20.** Time traces of a METIS simulation of EAST two-frequency LH discharge.

during application of the LH power using a coarse scaling law for the CD efficiency determined from LH experiments in TS tokamak [49], may be ascribed (for example) to the existence of a population of runaway electrons generated in the start-up phase of the discharge. Consistently, using LUKE or CQL3D FP codes, the predicted current in the Ohmic phase is far too low ( $<200$  kA) as compared to observation using the experimentally measured  $V_{\text{loop}} = 0.8$  V and  $Z_{\text{eff}} \approx 2.0$ , while the predicted current level is rather close to experimental value  $I_p = 430$  kA, when  $V_{\text{loop}}$  is twice larger, close to the value determined by METIS code. If one considers error bars on the electron temperature and  $Z_{\text{eff}}$  measurements it is possible to increase the peak electron temperature from 0.9 to 1.0 keV to  $\sim 1.2$  keV and reduce  $Z_{\text{eff}}$  from 2.0 to  $\sim 1.8$ , in which case the predicted ohmic current from LUKE and CQL3D increases to  $\sim 370$  kA, which is much closer to the experimental value of 430 kA.

From C3PO/LUKE calculations, the loop voltage at 4.15 s and 5.15 s are evaluated to match the experimental plasma current  $I_p = 430$  kA and  $Z_{\text{eff}} (=2.8$  at 4.15 s and  $=3.0$  at 5.15 s), taking into account of synergistic effects. The electric field profile is taken flat over the plasma. With the 2.45 GHz antenna,  $V_{\text{loop}} = 0.7$  V (close to METIS code value), while  $V_{\text{loop}} = 0.58$  V for the 4.6 GHz antenna. The drop of loop voltage of the order of 0.12 V is consistent with observation and the total plasma current is well retrieved.

Power absorption and current density profiles at 4.15 s and 5.15 s are displayed in figures 21(a) and (b). Since power absorption is more off-axis with the 4.60 GHz antenna, the

internal inductance is found to be lower as compared to the one corresponding to 2.45 GHz, which is not consistent with observations. However, the detailed characteristic of the current density profiles in the outermost part of the plasma is usually difficult to model, leading to a large uncertainty on the predicted internal inductance level. Nevertheless, the order of magnitude of the measured value is rather well recovered by calculations, especially considering how sensitive the internal inductance is to variations in the current density profile at large radii ( $0.6 < r/a < 1.0$ ).

Uncertainties in the measurement of  $Z_{\text{eff}}$  have already been discussed earlier in terms of how they can impact the predictions of plasma current during the Ohmic phase. Such uncertainties can also affect discharge simulations during the phase with LHCD injection. For example figure 22 shows the predictions of LHCD from GENRAY/CQL3D with 2.45 GHz power (4.15 s) and 4.6 GHz power (5.15 s), where now  $Z_{\text{eff}} = 2.1$  (near its Ohmic value) has been assumed and the actual experimental values of loop voltage were used at 4.15 s ( $V_{\text{loop}} = 0.27$  V) and at 5.15 s ( $V_{\text{loop}} = 0.15$  V). In this case the integrated LH currents at 2.45 GHz and 4.6 GHz were found to be 460 kA and 416 kA respectively, thus the RT/Fokker Planck model was found to approximately give the experimental current of 430 kA sustained with both LH systems using the experimental loop voltages and a lower  $Z_{\text{eff}}$ . If the same  $Z_{\text{eff}}$  is used as that in figure 21, we find the total (LH plus Ohmic) current drops by about 20%. Although the total current predicted by LUKE/C3PO and GENRAY/CQL3D are different in magnitude, the conclusion is the same from both

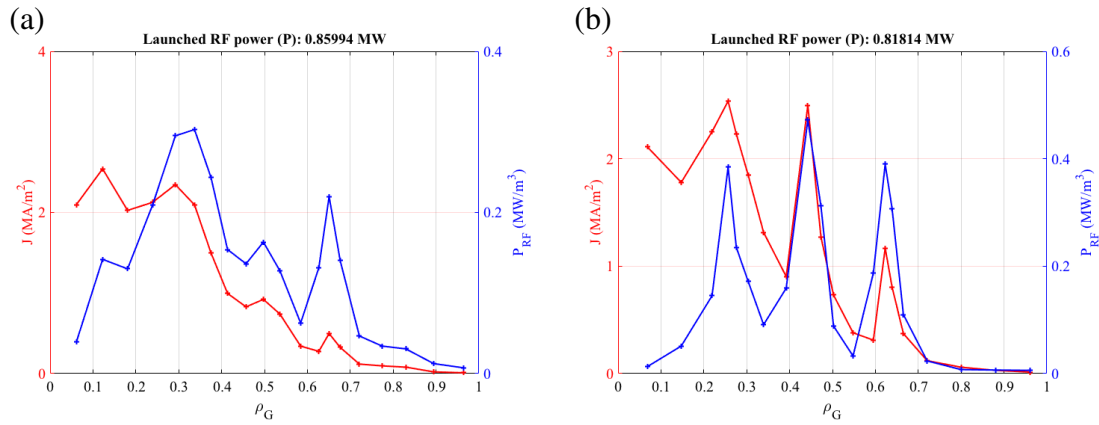


**Figure 21.** (a) Power absorption and current density profiles for the 2.45 GHz antenna evaluated by C3PO/LUKE codes. The calculated internal inductance is about 1.53, while experimental value is 1.25 approximately. (b) Power absorption and current density profiles for the 4.6 GHz antenna evaluated by C3PO/LUKE codes. The calculated internal inductance is about 1.31, while experimental value is 1.3 approximately.

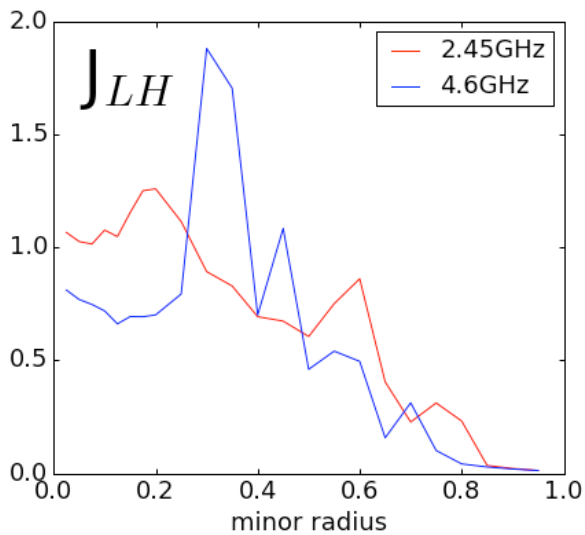


**Figure 22.** GENRAY/CQL3D simulation of EST two-frequency LHCD discharge #54439. LH current density profiles versus normalized radius. Red curve corresponds to 2.45 GHz injection at 4.15 s and blue curve corresponds to 4.6 GHz injection at 5.15 s.

models, namely the total current from ohmic and LH is comparable for both the 2.45 GHz and 4.6 GHz systems.

The study of the two-frequency EAST LH discharge has highlighted the need to perform time dependent simulations prior to detailed time slice studies, in order to cross-check the veracity of the discharge, i.e. the consistency between quantities that play a critical role in CD calculations. In particular, the ability to reproduce an Ohmic phase is essential to validate further LH discharges with non-negligible residual loop voltage. The procedure here considered, using ALOHA code for power spectra, METIS code for global discharge simulation, and ultimately C3PO/LUKE and GENRAY/CQL3D for CD calculations, demonstrates the importance of verifying the self-consistency of input data that one employs in such analyses. In addition, the variation of measured quantities within error bars was also found to be important, e.g. the variation of  $Z_{\text{eff}}$ .

In a next step, fully self-consistent calculations between toroidal MHD equilibrium and ray-tracing/FP must be carried out. If the predicted current density profile with is far from the equilibrium one, the convergence, if any, may take a rather long time.

#### 4. Conclusions and discussion

Experimental and simulation/modeling results have been presented for LHCD in discharges on the Alcator C-Mod, EAST, and JET tokamaks. Taken together these results represent significant progress in understanding LHCD at densities where off-axis current profile control would be needed in the ITER device and beyond. Although these experiments were carried out over a wide range of density (factor of ten) and toroidal magnetic field (factor of five) they can all be meaningfully compared with each other in terms of the dimensionless parameter ( $f_{pe}/f_{ce}$ ) which determines wave accessibility and wave refraction (see figure 1). The primary challenge in understanding these experiments is they all occur in electron temperature regimes where the LH wave is not fully absorbed in a single pass into the plasma core and thus the role of the scrape off layer (SOL) in determining wave propagation and parasitic losses must be taken into account. A second challenge in understanding these experiments is including time dependent physics in the modeling such as the evolving role of the DC electric field as the current density profile evolves towards a stationary state. Furthermore a fully self-consistent prediction of the current by combined RT/Fokker Planck and tokamak solvers like METIS/TRANSP must be carried out systematically.

Experiments carried out in EAST (see figure 8) demonstrate the importance of SOL conditions in weak absorption regimes by comparing the efficiency of LHCD in discharges with weak and strong lithiation. Presumably in these experiments, consistent with previous results [7, 8], strong lithiation reduces the wall recycling of neutrals, the edge temperature is increased and the effect of PI and CA is reduced, which

is beneficial for improving CD efficiency. Results from the Alcator C-Mod tokamak (see figure 7) demonstrate the CD effect can be recovered at high density by increasing the plasma current from  $\sim 0.6$  to  $0.8$  MA up to  $1.0$  MA. Higher current in C-Mod significantly decreases the scrape off layer width which places the slow wave cut-off much closer to the LCFS thus minimizing the distance the LH wave may traverse in the SOL. Measurements of nonthermal ECE and hard x-ray emission in the JET device with LH power applied at high density indicate a similar loss in the CD effect as was observed in EAST and C-Mod. Analysis of the JET experiments indicates that in addition to the onset of PI, loss of wave accessibility could be an issue in these discharges. It is important to point out however that electron temperatures in a burning plasma such as ITER will be high enough to easily guarantee strong single pass damping of LH waves, thus minimizing parasitic SOL interactions, such as CA and parametric decay instabilities, unless parasitic SOL interaction occurs at the very first pass when the wave is launched.

A unique feature of the EAST facility is the capability to study LHCD using two different LH source frequencies ( $2.45$  and  $4.6$  GHz) in the same discharge. Experiments carried out on EAST indicate improved CD efficiency at  $4.6$  GHz. Detailed modeling analysis that combines the ALOHA coupling code with the RT/Fokker Planck codes LUKE/C3PO and GENRAY/CQL3D indicates this improvement can be attributed primarily to an increased power fraction in the main co-CD lobe of the LH waveguide launcher at  $4.6$  GHz relative to  $2.45$  GHz (see figure 18) as well as a reduction in the growth rate of PI (see figures 16 and 17). The capability to apply higher frequency LH power ( $4.6$  GHz) in EAST, thus avoiding PI at higher density, has also allowed the achievement of high performance, long pulse, H-mode discharges where the plasma current is partially maintained by LHCD at  $B_0 = 2.8$  T and line averaged densities of  $\sim 4.5 \times 10^{19} \text{ m}^{-3}$  (see figure 5). Note that in these experiments the higher toroidal field is important for maintaining LH wave accessibility in the higher density H-mode.

The wide range of discharge conditions under which the LHCD experiments of this joint study were performed, as well as improvements in edge diagnostics, has motivated a number of innovations in the modeling and simulation tools that were applied to analyze these experiments as part of this joint study. In particular the idea of broadening the initial power spectrum up to values of  $N_{//}$  near the electron Landau limit was found to yield better agreement between the measured and simulated profiles of hard x-ray emissivity in the TS, Alcator C-Mod, and EAST tokamaks (see figures 9 and 10). It has been proposed that this spectral broadening could occur via scattering of the LH waves from density fluctuations in the SOL or from nonlinear PI. A new model for the density and temperature profiles in the SOL based on density/temperature measurements at the divertor plates and midplane in Alcator C-Mod was implemented in a RT package where it was shown that the dramatic increase in collisional damping of rays that reached the cold dense divertor area could explain the density limit observed during LHCD in C-Mod (see figure 11). A new RT/Fokker Planck package was also developed, which includes

real 2D geometry accounting for the plasma boundary and launcher shape and a new 3D relativistic bounce averaged FP code, and was applied to JET discharges in order to understand the effect of spectral broadening on nonthermal ECE and hard x-ray emission during LHCD. A central conclusion in this study from a statistical analysis of ray behavior was that the initial power spectrum is upshifted in  $N_{//}$  for both low and high density discharges that were analyzed, however the upshift is significantly more pronounced at high density where rays were found to propagate farther and undergo more reflections before being absorbed.

Finally a detailed time dependent analysis was carried using the METIS code for both the ohmic and LH driven current phases of a discharge in EAST (see figure 3) where two different frequency LH sources were applied. The motivation behind this analysis was primarily to determine the self-consistency between measurements of plasma current, loop voltage (and thus DC electric field), plasma charge state, plasma density, and electron and ion temperatures. It is well-known the LH CD is a highly nonlinear function of the DC electric field, especially at lower density, and thus uncertainties in DC electric field,  $Z_{\text{eff}}$ , and electron temperature can profoundly impact the final predictions of LH CD. It is worth noting that similar time dependent analysis was carried out using another integrated modeling suite (TRANSP + GENRAY + CQL3D) to assess how uncertainties in experimentally measured quantities affected LHCD predictions in Alcator C-Mod [50].

In conclusion, although achieving a complete understanding of the physics of LH wave propagation and absorption in present day devices is indeed a challenging problem, the prospects for application of off-axis LH CD in a reactor grade plasma are quite promising from the standpoint of core wave physics and minimal scrape off layer interactions. The key ingredients for successful application of LHCD in a reactor will be high enough electron temperature to guarantee strong single pass damping, high enough wave frequency to avoid PI, and a quiescent scrape off layer to minimize scattering from density fluctuations.

## Acknowledgments

This work is supported by the National Magnetic Confinement Fusion Science Program of China (Grant No. 2015GB102003, 2013GB106001B, 2013GB112003, 2015GB101002), the National Natural Science Foundation of China (Grant No. 11675214, 11175206, 11305211 and 11275233), the National Key R&D Program of China (Grant No. 2016YFA0400600, and 2016YFA0400602), Hefei Science Center CAS (2016HSC-IU008), the JSPS-NRF-NSFC A3 Foresight Program in the field of Plasma Physics (NSFC No. 11261140328), and K C Wong Education Foundation. Part of the work was conducted on the Alcator C-Mod tokamak, a DoE Office of Science user facility, and is supported by USDoE awards DE-FC02-99ER54512, DE-AC02-09CH11466, and DoE Grant DE-SC0010492. It is partly supported by the China-Italy and the China-France Collaboration program. We also give thanks to the support from the IOS TG of the ITPA.

This work has been carried out within the framework of the EUROfusion Consortium and has received funding from the Euratom research and training programme 2014-2018 under grant agreement No 633053. The views and opinions expressed herein do not necessarily reflect those of the European Commission. Work has been part-funded by the RCUK Energy Programme (grant number EP/P012450/1).

## ORCID iDs

M. Li  <https://orcid.org/0000-0002-3658-8243>

## References

- [1] Decker J. *et al* 2011 *Nucl. Fusion* **51** 073025
- [2] Cesario R. *et al* 2013 *Plasma Phys. Control. Fusion* **55** 045005
- [3] Gormezano C. *et al* 2007 *Nucl. Fusion* **47** S285
- [4] Litaudon X. *et al* 2002 *Plasma Phys. Control. Fusion* **44** 1057
- [5] Giruzzi R. *et al* 2015 *Nuclear Fusion* **55** 073002
- [6] Cardinali A. *et al* 2018 *Sci. Rep.* **8** 10318
- [7] Cesario R. *et al* 2010 *Nat. Commun.* **1** 55
- [8] Cesario R. *et al* 2004 *Phys. Rev. Lett.* **92** 175002
- [9] Bonoli P.T. and Englade R. C. 1986 *Phys. Fluids* **29** 2937
- [10] Peysson Y. *et al* 2011 *Plasma Phys. Control. Fusion* **53** 124028
- [11] Bonoli P.T. and Ott E. 1982 *Phys. Fluids* **25** 359
- [12] Fisch N.J. and Boozer A.H. 1980 *Phys. Rev. Lett.* **45** 720
- [13] Baek S.G. *et al* 2016 *Phys. Plasmas* **23** 050701
- [14] Madi M. *et al* 2015 *Plasma Phys. Control. Fusion* **57** 125001
- [15] Hillairet J. *et al* 2010 *Nucl. Fusion* **50** 125010
- [16] Liu F.K. *et al* 2015 *Nucl. Fusion* **55** 123022
- [17] Li M.H. *et al* 2016 *Phys. Plasmas* **23** 102512
- [18] Ding B.J. *et al* 2017 *Nucl. Fusion* **57** 022022
- [19] Lyu B. *et al* 2014 *Rev. Sci. Instrum.* **85** 11E406
- [20] Faust I. *et al* 2016 *Phys. Plasmas* **23** 056115
- [21] Peysson Y. and the TORE SUPRA Team 2000 *Plasma Phys. Control. Fusion* **42** B87–114
- [22] Baek S.G. *et al* 2015 *Nucl. Fusion* **55** 043009
- [23] Castaldo C. *et al* 2016 *Nucl. Fusion* **56** 016003
- [24] Goniche M. *et al* 2015 *Edge Plasma-Lower Hybrid Wave Interaction and Current Drive Efficiency 42nd EPS Conf. (Lisbon, Portugal, 22–26 June)* (<http://ocs.ciemat.es/EPS2015PAP/pdf/P2.138.pdf>)
- [25] Cesario R. *et al* 2011 *Plasma Phys. Control. Fusion* **53** 085011
- [26] Wallace G.M. *et al* 2010 *Phys. Plasma* **17** 082508
- [27] Barbato E. *et al* 2014 *Nucl. Fusion* **54** 123009
- [28] Ding B.J. *et al* 2013 *Nucl. Fusion* **53** 113027
- [29] Peysson Y. *et al* 2016 *Plasma Phys. Control. Fusion* **58** 044008
- [30] Peysson Y. *et al* 2012 *Plasma Phys. Control. Fusion* **54** 045003
- [31] Mungarrd B. *et al* 2015 *Bull. Am. Phys.* **60** CP12.019
- [32] Decker J. *et al* 2014 *Phys. Plasmas* **21** 092504
- [33] Peysson Y. *et al* 2008 *Theory of fusion plasmas AIP Conf. Proc.* **1069** 176
- [34] Smirnov A.P. and Harvey R. 1995 *Bull. Am. Phys. Soc.* **40** 1837
- [35] Harvey R.W. and McCoy M. 1992 *The CQL3D Fokker–Planck code Proc. IAEA Technical Committee Meeting on Simulation and Modeling of Thermonuclear Plasmas pp 489–526* (<https://mendeley.com/research-papers/cql3d-fokker-planck-code/>)
- [36] Shiraiwa S. *et al* 2015 *AIP Conf. Proc.* **1689** 030016
- [37] Wallace G.M. *et al* 2012 *Phys. Plasmas* **19** 062505
- [38] Kirov K. *et al* 2016 *Plasma Phys. Control. Fusion* **58** 125001
- [39] Kirov K. *et al* 2010 *Nucl. Fusion* **50** 075003
- [40] Kirov K. *et al* 2012 *Plasma Phys. Control. Fusion* **54** 074003
- [41] Cesario R. *et al* 2014 *Nucl. Fusion* **54** 043002
- [42] Takase Y. and Porkolab M. 1983 *Phys. Fluids* **26** 2992
- [43] Baek S.G. *et al* 2014 *Phys. Plasmas* **21** 061511
- [44] Porkolab M. 1977 *Phys. Fluids* **20** 2058
- [45] Liu C.S. *et al* 1984 *Phys. Fluids* **27** 1709
- [46] Nilsson E. *et al* 2013 *Nuclear Fusion* **53** 083018
- [47] Peysson Y. and Decker J. 2014 *Fusion Sci. Technol.* **65** 22–43
- [48] Artaud J.F. *et al* 2010 *Nuclear Fusion* **50** 043001
- [49] Goniche M. *et al* 2005 *16th topical conference on radio frequency power in plasmas AIP Conf. Proc.* **787** 307–10
- [50] Poli F.M. *et al* 2016 *Plasma Phys. Control. Fusion* **58** 095001
- [51] Peysson Y. *et al* 2017 *EPJ Web Conf.* **157** 02007
- [52] Litaudon X. *et al* 2017 *Nucl. Fusion* **57** 102001